AGU PUBLICATIONS

JGR

Journal of Geophysical Research: Space Physics

RESEARCH ARTICLE
10.1002/2015JA021396

Key Points:
- Average energy estimate from optical neutral temperature observations
- Updated Hall conductance relations
- Characterizing auroral electron precipitation parameters and conductance

Correspondence to:
S. R. Kaeppler,
stephen.kaeppler@sri.com

Citation:
Kaeppler, S. R., D. L. Hampton, M. J. Nicolls, A. Strømme, S. C. Solomon, J. H. Hecht, and M. G. Conde (2015), An investigation comparing ground-based techniques that quantify auroral electron flux and conductance, *J. Geophys. Res. Space Physics*, *120*, 9038–9056, doi:10.1002/2015JA021396.

Received 29 APR 2015
Accepted 22 SEP 2015
Accepted article online 28 SEP 2015
Published online 26 OCT 2015

An investigation comparing ground-based techniques that quantify auroral electron flux and conductance

S. R. Kaeppler[1], D. L. Hampton[2], M. J. Nicolls[1], A. Strømme[1], S. C. Solomon[3], J. H. Hecht[4], and M. G. Conde[2]

[1]SRI International, Menlo Park, California, USA, [2]Geophysical Institute, University of Alaska Fairbanks, Fairbanks, Alaska, USA, [3]High Altitude Observatory, National Center for Atmospheric Research, Boulder, Colorado, USA, [4]The Aerospace Corporation, Los Angeles, California, USA

Abstract We present three case studies that examine optical and radar methods for specifying precipitating auroral flux parameters and conductances. Three events were chosen corresponding to moderate nonsubstorm auroral activity with 557.7 nm intensities greater than 1kR. A technique that directly fits the electron number density from a forward electron transport model to alternating code incoherent scatter radar data is presented. A method for determining characteristic energy using neutral temperature observations is compared against estimates from the incoherent scatter radar. These techniques are focused on line-of-sight observations that are aligned with the local geomagnetic field. Good agreement is found between the optical and incoherent scatter radar methods for estimates of the average energy, energy flux, and conductances. The Pedersen conductance predicted by Robinson et al. (1987) is in very good agreement with estimates calculated from the incoherent scatter radar observations. However, we present an updated form of the relation by Robinson et al. (1987), $\Sigma_H/\Sigma_P = 0.57\langle E\rangle^{0.53}$, which was found to be more consistent with the incoherent scatter radar observations. These results are limited to similar auroral configurations as in these case studies. Case studies are presented that quantify auroral electron flux parameters and conductance estimates which can be used to specify the magnitude of energy dissipated within the ionosphere resulting from magnetospheric driving.

1. Introduction

Precipitating electrons and the resulting currents associated with auroral activity are important for magnetospheric-ionospheric coupling because they deposit and dissipate heat, energy, and momentum into the thermosphere, respectively. Electron interaction with the thermosphere causes ionization and excitation of thermospheric oxygen and nitrogen. This consequently causes visible auroral emissions and ionization, which enhances the local background electron number density and ionospheric conductivity. Ionospheric currents flow within these regions of enhanced ionospheric conductivity, and energy is dissipated through Joule heating. Thus, specification of precipitating electron flux is of fundamental importance for quantifying energy dissipation in magnetospheric-ionospheric coupling. Two quantities are typically used to specify the precipitating electron flux: the characteristic (average) energy and the energy flux.

Incoherent scatter radar (ISR) has played a critical role in ground-based specification of precipitating electron flux in a localized sense, because ISR provides height-resolved measurements of the electron number density. Although ISR cannot directly sense the enhanced ionization, measurements of backscattered power are directly related to the electron number density [*Vickrey et al.*, 1982]. The electron spectra can be inferred by inverting measurements of enhanced electron number density, provided that there is an appropriate forward model that describes how precipitating electrons generate ionization. Casting the problem into a matrix form [*Brekke et al.*, 1989],

$$q(z) = \sum_E \mathbf{A}(E,z)\phi(E)\Delta E \tag{1}$$

where $q(z)$ is the height ionization. The electron spectrum, $\phi(E)$, is determined by inverting $\mathbf{A}(E,z)$. The kernel, $\mathbf{A}(E,z)$, is calculated using a forward height ionization model [e.g., *Rees*, 1963] as a function of altitude and energy. An early inversion technique named "UNTANGLE" was developed by *Vondrak and Baron* [1977]. This method is iterative where ionization at the highest energy bin is calculated first, and each subsequent

energy bin relies on the estimate from the previous energy bin. Since it was possible for uncertainty to propagate, this method is prone to errors [*Brekke et al.*, 1989; *Semeter and Kamalabadi*, 2005]. *Brekke et al.* [1989] obtained a solution to $\phi(E)$ by minimizing the difference between the observed height ionization profile obtained by the European Incoherent Scatter (EISCAT) radar system and forward model results using a least squares approach. The program developed by *Brekke et al.* [1989] is called "CARD," and a similar program called "SPECTRUM" [*Kirkwood*, 1988] was also developed for inverting EISCAT ISR data. *Gattinger et al.* [1991] showed that the model by *Strickland et al.* [1989] and UNTANGLE produced similar estimates of the energy flux and somewhat similar estimates of the average energy for an auroral event observed on 28 February 1987 as part of a coordinated observation effort at Sondrestrom, Greenland. *Strickland et al.* [1994] expanded upon the study by *Gattinger et al.* [1991] and presented results of the energy flux and average energy for four additional auroral events observed on 28 February 1987. *Strickland et al.* [1994] directly fit a three-species transport model [*Strickland et al.*, 1993; *Basu et al.*, 1993] to the ISR electron number density observations. They found that diffuse aurora was best fit by a Maxwellian electron distribution and discrete aurora was best fit to a Gaussian electron distribution. *Doe et al.* [1997] solved equation (1) using the method of singular value decomposition [*Press et al.*, 2007], but this approach suffers from issues, such as the output of negative electron fluxes.

More recently, *Semeter and Kamalabadi* [2005] employed a method for inverting **A** by using a maximum entropy method (MEM), which maximizes the Burg entropy. *Semeter and Kamalabadi* [2005] applied this method to observations from the Sondrestrom ISR, and *Jones et al.* [2009] applied this method to observations from the Poker Flat Incoherent Scatter Radar (PFISR) during pulsating aurora. Both studies produced good estimates of the electron flux. *Simon Wedlund et al.* [2013] recently revisited this method to assist in a combined ISR and tomographic study of discrete auroral events observed by the EISCAT ISRs. They showed that the multiplicative algebraic reconstruction technique (MART) and MEM could be applied to ISR data, with consistent estimates of the electron spectra being produced by both techniques. However, MEM produced smooth results, whereas MART electron flux estimates showed more variations.

Using the electron deposition model by *Rees* [1963] and assuming a Maxwellian flux distribution, *Vickrey et al.* [1981] developed an empirical model that connected the characteristic energy and energy flux to the Hall and Pedersen conductances. The empirical results from *Vickrey et al.* [1981] were further expanded and applied to satellite studies in which the energy flux and characteristic energy could be determined from satellite-based electron spectra measurements [*Wallis and Budzinski*, 1981; *Harel et al.*, 1981; *Spiro et al.*, 1982]. The empirical relation took the form

$$\Sigma_P = \frac{A_P E_0}{B_P + E_0^2} Q_0^{\alpha} \tag{2}$$

and

$$\frac{\Sigma_H}{\Sigma_P} = A_H E_0{}^{\beta} \tag{3}$$

where A_P, B_P, and A_H are constants, $\alpha \approx 0.5$, $\beta \approx 0.3$–0.8, and E_0 and Q_0 are the characteristic energy and energy flux, respectively. This relation was revised by *Robinson et al.* [1987] (hereafter referred to as the "Robinson relation") to include a rigorous definition of average energy, $\langle E \rangle$, and corrections for electron detector energy range effects. *Robinson et al.* [1987] applied this relation and showed good agreement between HILAT satellite observations and data from the Sondrestrom ISR. This relation was applied to a statistical study of 14 million DMSP spectra by *Hardy et al.* [1987]. An alternative empirical model of conductance was developed by *Reiff* [1984] who refit the results from *Vickrey et al.* [1981] and *Wallis and Budzinski* [1981], which expressed the Hall and Pedersen conductances as two polynomial fits, depending on the characteristic energy.

The other primary ground-based method for determining the energy flux and characteristic energy of precipitating auroral electrons is through optical observations. Determining optical emissions using an incident electron flux has recently been reviewed by *Lanchester and Gustavsson* [2012] and *Semeter and Zettergren* [2014]. *Dalgarno et al.* [1965] established that the intensity of the first negative emission band for N_2^+ at 427.8 nm was proportional to the incident energy of an electron beam and thus could be used as a proxy for the energy flux of precipitating auroral electrons. Modeling studies by *Rees and Luckey* [1974] derived a conversion factor of approximately 210 R/mW/m^2. *Kasting and Hays* [1977] used ground- and space-based

data from the Atmospheric Explorer D satellite to obtain a conversion of 256 ± 125 R/mW/m^2. Recently, *Lanchester et al.* [1997] used the *Lummerzheim and Lilensten* [1994] model to obtain a conversion estimate ranging from 220 to 280 R/mW/m^2.

Determining the characteristic energy via optical emissions is a more challenging task. *Rees and Luckey* [1974] developed a technique that used the ratio of 630.0 nm to 427.8 nm emission to determine the characteristic energy. This "red-to-blue" ratio method has the limitation that it is valid for stable aurora, considering that the radiative transition time for the 630.0 nm emission line is approximately 110s [*Chamberlain*, 1961]. *Hecht et al.* [2006] presented a short review of the "red-to-blue" ratio method, along with an updated method that used 427.8 nm, 630 nm, 844.6 nm, and 871.0 nm emission lines to estimate average energy. They also showed the importance of using 844.6 nm and 871.0 nm emission to constrain compositional changes that can influence the estimate of average energy [*Hecht et al.*, 2006]; the effect of O composition on the average energy was previously examined by *Hecht et al.* [1989]. More recently, many studies have focused on other transitions, with an emphasis on "prompt" auroral emissions [*Semeter et al.*, 2001; *Tuttle et al.*, 2014, and references therein]. A commonly used set of prompt emitters for determining the characteristic energy associated with dynamic aurora is the ratio between 562.0 nm and 777.4 nm emissions, caused by transitions of O_2^+ and O, respectively [*Dahlgren et al.*, 2008; *Lanchester et al.*, 2009; *Dahlgren et al.*, 2011; *Lanchester and Gustavsson*, 2012; *Tuttle et al.*, 2014; *Dahlgren et al.*, 2015].

Hecht et al. [2006] put forth a method for determining characteristic energy which makes use of neutral temperature measurements from scanning Doppler imaging Fabry-Perot interferometers (hereafter referred to as "SDI") [*Conde and Smith*, 1995, 1997; *Anderson et al.*, 2013]. Among other emissions, the SDI measures the 557.7 nm emission in order to infer the *E* region neutral winds and temperatures. Precipitating electrons with higher characteristic energies penetrate deeper into the thermosphere, causing a decrease in the neutral temperature estimated from the line width of 557.7 nm emission [*Rees*, 1989; *Holmes et al.*, 2005; *Hecht et al.*, 2006]. This effect is observed in the SDI and can be used to determine the neutral temperature in 115 azimuth/elevation sectors in the sky, thus enabling estimates of the characteristic energy over the whole sky. An upcoming companion paper will describe the technique for determining characteristic energy from SDI observations.

We seek to specify electron precipitation, conductance, and the local ionospheric response associated with auroral particle precipitation using ground-based techniques, specifically ISR and optical measurements. In this paper, we present a technique for estimating the energy flux and characteristic (average) energy of precipitating auroral electrons by directly fitting the electron number density produced by the GLOW forward electron transport model with the ISR electron number density observations, similar to the methods used by *Brekke et al.* [1989] and *Strickland et al.* [1994]. For simplicity, we restrict our focus to observations aligned with the geomagnetic field. We compare the ISR parameter estimates with the results from the SDI and all-sky imager, probing a similar field of view. We use the estimates from the ISR to experimentally test the Robinson relation, since those formulas connect characteristic energy and energy flux with the Hall and Pedersen conductances. Although we restrict our attention to the look direction aligned with the local geomagnetic field, we use these results as a first step toward developing techniques for examining line-of-sights which are not aligned with the geomagnetic field. New imaging modes enable ISR to be able to sample in the zonal and meridional directions, nearly simultaneously for the first time [*Heinselman and Nicolls*, 2008; *Semeter et al.*, 2009; *Butler et al.*, 2010; *Nicolls et al.*, 2014].

2. Radar and Optical Observations

2.1. Incoherent Scatter Radar Observations

Observations were obtained using the Advanced Modular Incoherent Scatter Radar (AMISR) located at the Poker Flat Research Range (65.13°N, 147.47°W), Alaska (hereafter referred to as "PFISR"), and the Sondrestrom ISR (66.98°N, 50.95°W). There are collocated all-sky imagers at both facilities, with filters for 427.8 nm, 557.7 nm, and 630.0 nm emission; these emissions are the dominant visible auroral emissions with their properties shown in Table 1 [*Chamberlain*, 1961; *Zettergren et al.*, 2007]. The red- (630.0 nm) and green-line (557.7 nm) emissions are dominant at the *F* and *E* regions, respectively, and the blue (427.8 nm) emission is a proxy for the energy flux. Sondrestrom also has additional filters for 777.4 nm and 750.0 nm emission (with properties not listed). The scanning Doppler imaging Fabry-Perot interferometer (SDI) is located at PFISR. AMISR is a phased-array, electronically steerable antenna that can form radar beams on the sky

Table 1. Properties of Dominant Auroral Emissions

Emission Wavelength	Transition	Transition Time	Proxy for:
427.8 nm	$N_2^+ \left(B^2\Sigma_u^+\right) \rightarrow N_2^+ \left(X^2\Sigma_u^+\right) + h\nu$	10^{-7} s	Energy flux
557.7 nm	$O(1^S) \rightarrow O(1^D) + h\nu$	0.74 s	*E* region ionization
630.0 nm	$O(1^D) \rightarrow O(3^P) + h\nu$	110 s	*F* region ionization

at a pulse-to-pulse cadence [*Kelly and Heinselman*, 2009; *Heinselman and Nicolls*, 2008]. For both radars the coverage of a given radar beam on the sky is approximately 1°.

Data were used from the radar beam that was aligned with the local geomagnetic field (at PFISR azimuth = −151° and elevation = 77.5°, and at Sondrestrom azimuth = 141° and elevation = 81°). This beam direction is best for observing field-aligned precipitating electrons that cause aurora; other radar line-of-sight (LOS) directions will slice through multiple magnetic flux tubes. We use standard alternating code (AC) ISR data products that have been fit to theoretical ISR power spectrum to estimate the plasma parameters as a function of altitude. Alternating code data were used for this study since the short pulse length of 30 μs provides high-range resolution at *E* region altitudes (≈ 4.5 km), enabling *E* region ionization to be resolved [*Heinselman and Nicolls*, 2008]. Alternating code data products used in this study are integrated with temporal resolutions of 180s and 60s at PFISR and Sondrestrom, respectively.

We selected auroral events based on the following criterion. First, the all-sky imager data must have > 1kR 557.7 nm green-line emission collocated with the field-aligned radar beam. Second, we focused on fairly stable aurora that remained in the field-aligned radar beam for many minutes; this condition is most consistent with the steady state assumption to be invoked. *Semeter and Kamalabadi* [2005] calculated characteristic time scales for ionization enhancements to be approximately 10–2s for 10^{11}–10^{12} m^{-3} at nominal *E* region altitudes, respectively. To be most consistent with the steady state assumption, the aurora should remain visually and spatially stable over a few of these characteristic time scales. For the events to be presented, this is almost always the case, although there may be intervals in which the aurora evolved more rapidly than the characteristic time scale, thus making the steady state assumption more questionable. However, for the presentation of the results, we have included all data.

2.2. Scanning Doppler Imager and Other Optics

The characteristic energy was derived from thermospheric neutral temperature observations acquired by the SDI, collocated with PFISR. The SDI makes all-sky observations and separates the Doppler neutral temperature observations into various "zones" on the sky; each zone has an individual fit of the observed airglow or auroral spectrum, from which the neutral wind velocity and temperature are determined. Observations are made for 557.7 nm and 630.0 nm wavelength, corresponding to *E* and *F* region airglow, respectively [e.g., *Chamberlain*, 1961]. The time cadence of these observations is approximately 2min, which forms a great complement to the ISR alternating code time cadence of 3min. The SDI instrument is discussed in *Conde and Smith* [1995, 1997] and *Anderson et al.* [2013].

Hecht et al. [2006] suggested a technique that can be used to infer the characteristic energy from the Doppler shift in the neutral temperature. It is assumed that precipitating auroral electrons come into thermal equilibrium with the thermosphere at a faster time scale than the instrument integration (< 3min). There is a nonlinear neutral temperature gradient between 80 and 200 km. Therefore, changes in the altitude of the auroral precipitation, corresponding to changes in the characteristic energy of the precipitating electron flux, result in nonlinear neutral temperature response. A lower observed thermospheric temperature can be caused by electrons with a high characteristic energy, while a higher observed thermospheric temperature can be caused by precipitating electrons with a lower characteristic energy [*Rees*, 1989; *Holmes et al.*, 2005; *Hecht et al.*, 2006]. A key feature in this technique is the use of a neutral atmosphere model, such as Mass Spectrometer Incoherent Scatter (MSIS) [*Picone et al.*, 2002] to specify the variation of the neutral temperature with altitude.

We present data from The Aerospace Corporation's four-channel optical photometer that is described in *Hecht et al.* [2006], which is collocated with PFISR. The four optical emissions that are observed by the photometer are 427.8 nm, 630.0 nm, 844.6 nm, and 871.0 (871.4) nm. The key data from this system to be presented are the 427.8 nm emission and the average energy. Further information about how the average energy is determined can be found in *Hecht et al.* [2006], although we note that the 427.8 nm and 630.0 nm emissions

are used in a fashion similar to the method by *Rees and Luckey* [1974], although the method by *Hecht et al.* [2006] accounts for effects from thermospheric composition changes.

3. Forward Models of the Volume Ionization Rate

3.1. Forward Models

As discussed by *Semeter and Kamalabadi* [2005], there are two approaches that can be applied to determine the volume ionization profile, $q(z)$, from precipitating auroral electrons. *Rees* [1963] used an experimentally derived range-energy relation [*Grün*, 1957; *Barrett and Hays*, 1976] to calculate the volume ionization rate. The other approach involves solving the Boltzmann electron transport equations, either using a two-stream form for electrons moving upwards and downwards along the field line [*Nagy and Banks*, 1970; *Banks et al.*, 1974; *Solomon et al.*, 1988] or using a multistream formulation [*Strickland et al.*, 1989; *Lummerzheim and Lilensten*, 1994]. Both approaches have been validated using full Monte Carlo calculations [*Solomon*, 2001].

The forward model using the range-energy relation (hereafter referred to simply as the "range-energy model") that we use corresponds to equation (8) in *Semeter and Kamalabadi* [2005],

$$q(z) = \int_{E_{\min}}^{E_{\max}} \frac{\Lambda\left[s(z)/R(E)\right]\rho(z)}{35.5R(E)}\Phi(Q_0, E_0, E)E\mathrm{d}E \tag{4}$$

where z is the altitude along the geomagnetic field. The experimentally derived range-energy function is $R(E)$ in equation (4), and we use the value derived by *Barrett and Hays* [1976]. The scattering depth along the geomagnetic field, $s(z)$, corresponds to the depth a particle penetrates as it moves in the neutral atmosphere and has units of mass-distance. We note that the stopping altitude is defined as the altitude along the field line where $s(z) = R(E)$. At this altitude the electron has lost enough energy through interactions with the thermosphere that it becomes indistinguishable from background electrons [*Kivelson and Russell*, 1995]. The universal energy dissipation function is the fraction of the electron's initial energy lost per distance of mass (neutral atmosphere) traversed and is represented as $\Lambda\left[s(z)/R(E)\right]$ in equation (4). Table 1 of *Semeter and Kamalabadi* [2005] is used for $\Lambda\left[s(z)/R(E)\right]$ and is not repeated here. The precipitating electron flux, $\Phi\left(Q_0, E_0, E\right)$, is a function of the energy flux and characteristic energy, Q_0 and E_0, respectively. Finally, $\rho(z)$ corresponds to the mass density of the neutral atmosphere model, for which we use MSIS00 model [*Picone et al.*, 2002].

We use the GLOW model as the forward electron transport model [*Solomon et al.*, 1988]. At the heart of GLOW is a two-stream transport code [*Nagy and Banks*, 1970; *Banks et al.*, 1974], which calculates the field-aligned upward and downward hemispherical fluxes as a function of energy and altitude. GLOW also has a chemistry model which contains excitation and ionization cross sections; thus, it is possible to calculate the ionization and the volume emission rates for 427.8 nm, 557.7 nm, 630.0 nm, and other optical emissions. Both the volume ionization and volume emission rates are calculated as a function of altitude. Thus, for a given incident electron flux profile, it is possible both to calculate the volume ionization rate and to simultaneously determine the visible emission rate from GLOW.

One common feature in both models is that the precipitating electron distribution must be prescribed. For the range-energy model and GLOW we use a Maxwellian distribution

$$\Phi(Q_0, E_0, E) = \frac{Q_0 A_0}{2E_0^3} E \exp\left[-\frac{E}{E_0}\right] \tag{5}$$

where Q_0 is the energy flux with units of mW/m^2, E_0 is the characteristic energy in units of eV, and A_0 is a conversion factor so the units of $\Phi(Q_0, E_0, E)$ are m^{-2} s^{-1} eV^{-1} [*Solomon et al.*, 1988; *Jursa et al.*, 1985]. A Maxwellian distribution of the form of equation (5) has been used by many authors to describe precipitating auroral electrons [e.g., *Strickland et al.*, 1989; *Jursa et al.*, 1985; *Fang et al.*, 2010; *Kaeppler et al.*, 2014, and references therein]. In some cases it is found that a Gaussian distribution is more appropriate for discrete aurora [*Strickland et al.*, 1989; *Jursa et al.*, 1985]. Recent observational evidence has suggested that the precipitating electron flux generating discrete aurora can be described by a kappa distribution function with a power law tail [*Ogasawara et al.*, 2006; *Fang et al.*, 2010; *Kaeppler et al.*, 2014]. One consequence of the power law tail is that it contains more flux at higher energies, allowing the electrons to penetrate deeper into the ionosphere and causing larger-magnitude Hall conductances. For simplicity, we restrict our focus to the Maxwellian distribution, which is a reasonable assumption and starting point for this study. We note that the kappa

distribution is a generalization of a Maxwellian distribution function that has a high-energy tail; in the limit that $\kappa \to \infty$ the kappa distribution becomes a Maxwellian distribution [*Vasyliunas*, 1968].

To make our results more robust and comparable with other studies, we choose to use the average energy versus the characteristic energy. The average energy is defined as follows [*Robinson et al.*, 1987]

$$\langle E \rangle = \frac{\int \Phi(Q_0, E_0, E) E \mathrm{d}E}{\int \Phi(Q_0, E_0, E) \mathrm{d}E} \tag{6}$$

where $\Phi(Q_0, E_0, E)$ is defined in equation (5). Characteristic energy is dependent upon the definition of the precipitating electron flux distribution, whereas the average energy is independent of the choice of the distribution and can be determined for any observed electron distribution, provided the distribution can be numerically integrated. For the case of the Maxwellian distribution in equation (5), $\langle E \rangle = 2E_0$ to good approximation up to characteristic energies of 10 keV for GLOW and the range-energy model. It can further be validated that integrating the numerator in equation (6) will produce the energy flux, Q_0.

3.2. Least Squares Fitting the Forward Model to ISR Data

Rather than solving for the electron spectrum, $\Phi(E_0, Q_0)$, using regularization techniques [e.g., *Semeter and Kamalabadi*, 2005; *Simon Wedlund et al.*, 2013], we take an alternative approach of adjusting parameters in a model spectra and fitting the model results directly to the ISR data. We use the Levenberg-Marquardt least squares fitting technique [*Press et al.*, 2007] to fit the model to the ISR observed electron number density. The electron density profile is the primary quantity that is determined from ISR power measurements. We assume that the volume ionization is primarily at *E* region altitudes, that it is in steady state, that convection is negligible, and that the dominant recombination is with molecular ions [*Brekke et al.*, 1989; *Semeter and Kamalabadi*, 2005]. Combining these assumptions, the electron continuity equation can be simplified to

$$N_{e\mathrm{FWD}}(z) = \sqrt{\frac{q(z)}{\alpha[T_e(z)]}} \tag{7}$$

with units of cubic meters where *z* corresponds to altitude along the geomagnetic field and $\alpha[Te(z)]$ is the temperature-dependent molecular recombination rate in the *E* region. When using the range-energy model, the electron temperature from ISR observations was used. Within GLOW the International Reference Ionosphere (IRI) model electron temperature profile is calculated and the resulting electron number density is fit directly to the ISR data. Alternatively, the ISR electron temperature and recombination rate can be used with the GLOW ionization profile; however, these were results were found to produce nearly the same estimates for the average energy and electron flux as using the GLOW internally calculated electron temperature. Using equation (7), we can recast this problem into a least squares form between the forward model (FWD) and the ISR observations of electron number density,

$$\chi^2_\nu = \frac{1}{\nu} \sum \frac{\left[N_{e\mathrm{ISR}}(z) - N_{e\mathrm{FWD}}(z)\right]^2}{\sigma^2_{N_{e\mathrm{ISR}}}} \tag{8}$$

where χ^2_ν is reduced chi-square and ν is the number of degrees of freedom in the fit. The energy flux and characteristic energy, Q_0 and E_0, are the parameters that are being fit, respectively. $N_{e\mathrm{ISR}}$ and $\sigma_{N_{e\mathrm{ISR}}}$ are the ISR alternating code electron density and uncertainty in the electron density (part of the standard ISR data products; see section 2.1), as a function of altitude along the geomagnetic field. In this formulation, any forward model that generates volume ionization can be used, although we restrict our attention to intervals when visible auroral emission is present.

At *E* region altitudes, the dominant ion species are NO^+ and O_2^+ [*Schunk and Nagy*, 2004]. We use molecular recombination rates from *Schunk and Nagy* [2004] for NO^+,

$$\alpha_{NO^+} = 4.0 \times 10^{-13} \left[\frac{300}{T_e(z)}\right]^{0.5} \tag{9}$$

and for O_2^+,

$$\alpha_{O_2^+} = 2.4 \times 10^{-13} \left[\frac{300}{T_e(z)}\right]^{0.70} \tag{10}$$

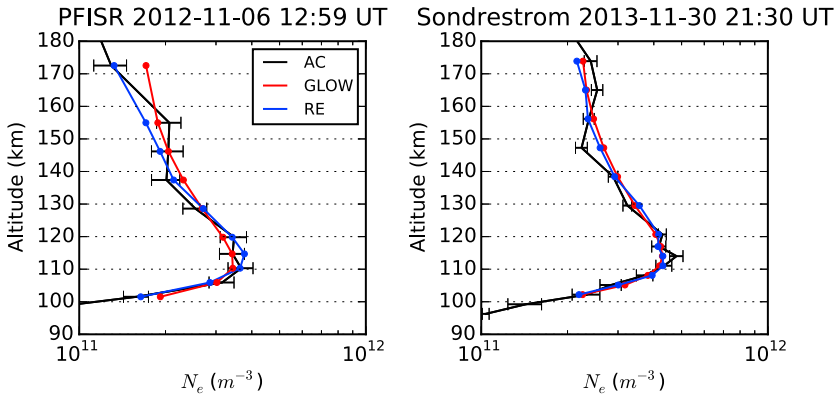

Figure 1. (left) Alternating code ISR data from PFISR versus the best fits using the GLOW model and the range-energy model at 1259 UT on 6 November 2012. Black is the alternating code data (AC) with error bars, red is the best fit to GLOW, and blue is the best fit range-energy model to the ISR data. (right) AC ISR data from the Sondrestrom ISR at 2130 UT on 30 November 2013 versus the best fit to GLOW and the range-energy model.

with units of m^3/s. An alternative approach is to use an altitude-only molecular recombination rate, such as the altitude-dependent rate put forth by *Vickrey et al.* [1982], $\alpha(z) = \alpha_0 \exp\left[-z/H\right]$, where H is the scale height for the recombination rate. *Semeter and Kamalabadi* [2005] show that the altitude-only recombination rate resided between pure NO^+ and pure O_2^+ concentrations. We do not use this altitude-only recombination rate in this work.

Above 180 km, the concentration of NO^+ and O_2^+ declines precipitously, as the dominant ion becomes O^+ [*Schunk and Nagy*, 2004]. Our model framework does not account for transport and thus is not valid above the region where chemical recombination is dominant. To be consistent with this constraint, alternating code data above 180 km are not used in our least squares fitting routine. We also placed a lower limit of 100 km onto the data. Electrons with characteristic energies in excess of 10 keV generate ionization at altitudes below 105 km [*Rees*, 1989; *Semeter and Kamalabadi*, 2005]. This range of characteristic energy would only be seen in the most active auroral events or pulsating aurora, which are not relevant for this study. For the PFISR data, a uniform 10% uncertainty was applied to the alternating code electron density profiles between 100 and 120 km, while above 120 km, the electron density profiles used uncertainties produced by the ISR fitting routine (σ_{Ne}). At the lower altitude bins, the uncertainty was generally < 10% which seemed optimistic; 10% was used as a more conservative estimate of uncertainty for the lowest altitude bins. To assist the algorithm toward the peak of the electron density profile, we used a Poisson weighting ($1/N_{e\mathrm{ISR}}$) versus a standard weighting Gaussian weighting ($1/\sigma^2_{Ne\mathrm{ISR}}$) in the fitting routine. This weighting was found to capture the peak of the electron density profile versus standard weighting.

We show two examples of the fitting routine using GLOW and the range-energy model with ISR data from PFISR and Sondrestrom. Figure 1 shows the AC ISR observations, the best fit using GLOW, and the best fit using the range-energy model. It is clear in these two cases that there is very good agreement between the ISR data and forward models. In Figure 1 (left), the fit by GLOW produced a reduced χ^2 value of 2.4 ($\chi^2_\nu = 2.4$) and the range-energy model had $\chi^2_\nu = 0.8$; the range-energy model clearly fits the data better. The Sondrestrom data in Figure 1 (right) had a value of $\chi^2_\nu = 0.8$ for GLOW and $\chi^2_\nu = 0.7$ for the range-energy model. In both cases, χ^2_ν for the number of degrees of freedom indicate that both fitted parameters were within the 99.99% confidence interval [*Bevington and Robinson*, 2003; *Kletzing et al.*, 1998]. For the PFISR example, the best fit estimate for the energy flux was $Q_0 = 7.3 \pm 0.8$ mW/m^2 and $Q_0 = 7.6 \pm 0.4$ mW/m^2 for the GLOW and range-energy models, respectively. The average energy estimates were $\langle E \rangle = 5.0 \pm 0.2$ keV and $\langle E \rangle = 5.6 \pm 0.4$ keV for GLOW and the range-energy model, respectively. In the Sondrestrom case shown in Figure 1 (right), the best fit GLOW model estimated $Q_0 = 11 \pm 0.5$ mW/m^2 and $\langle E \rangle = 4.2 \pm 0.2$ keV. The parameter uncertainty estimates correspond to 1σ error estimates produced internally in the Levenberg-Marquardt fitting routine [*Bevington and Robinson*, 2003].

3.3. Hall and Pedersen Conductances

We calculate the conductance using the observed ISR electron number density, which enables us to make direct comparisons between the energy flux and average energy with the Hall and Pedersen conductances. We use the Pedersen conductivity [e.g., *Evans et al.*, 1977],

$$\sigma_P(z) = \frac{eN_{eISR}(z)}{B(z)} \sum_i C_i \sum_j \left[\frac{\nu_{ij}/\Omega_i}{1 + \left(\frac{\nu_{ij}}{\Omega_i}\right)^2} + \frac{\nu_{en}/\Omega_e}{1 + \left(\frac{\nu_{ej}}{\Omega_e}\right)^2} \right] \tag{11}$$

and an approximate form for the Hall conductivity valid above 100 km [*Boström*, 1964],

$$\sigma_H(z) = \frac{eN_{eISR}(z)}{B(z)} \sum_i C_i \sum_j \frac{1}{1 + \left(\frac{\Omega_i}{\nu_{ij}}\right)^2} \tag{12}$$

where both the Hall and Pedersen conductivities are defined as a function of altitude (z) along the geomagnetic field. The summation is over the ith ion species and the jth neutral species. For the ion-neutral collision frequency, ν_{ij}, we use equation (7) from *Evans et al.* [1977],

$$\nu_{ij} = 1.546^{-16} N_j(z) \left(\frac{Z_j}{Z_i + Z_j}\right) \sqrt{\left(\frac{T_i(z)}{Z_i} + \frac{T_j(z)}{Z_j}\right)} \tag{13}$$

where N_j is the neutral species from the MSIS00 model with units of cubic meters, Z_k corresponds to the atomic number for the kth ion or neutral species, T_k corresponds to the temperature in kelvin for the kth ion or neutral species, and the constant at the front of the equation has units of $m^3\ s^{-1}\ K^{-1/2}$. The electron-neutral collision frequency is defined by equation (5) in *Evans et al.* [1977] as $\nu_{en} = 5 \times 10^{-4} N_n T_e^{1/2}$, where N_n is the total neutral number density in units of cubic meters. Ω_i and Ω_e correspond to the ion and electron gyrofrequencies, respectively. Further details regarding this implementation can be found in [*Kaeppler*, 2013], with the main difference here being that we use the observed ISR parameters instead of IRI model parameters.

We also estimate the Hall and Pedersen conductances using the relationship in *Robinson et al.* [1987], driven by best fit average energy and energy flux. The Robinson relation for the Pedersen conductance is

$$\Sigma_P = \frac{40\langle E \rangle}{16 + \langle E \rangle^2} Q_0^{1/2} \tag{14}$$

and for the Hall conductance

$$\Sigma_H = 0.45 \langle E \rangle^{0.85} \Sigma_P \tag{15}$$

where $\langle E \rangle$ is the average energy. We also propagate the 1σ uncertainties through equations (14) and (15) to obtain

$$\left(\frac{\Delta\Sigma_P}{\Sigma_P}\right)^2 = \left(1 - \frac{2\langle E \rangle^2}{16 + \langle E \rangle^2}\right)^2 \left(\frac{\Delta\langle E \rangle}{\langle E \rangle}\right)^2 + \left(\frac{1}{2}\right)^2 \left(\frac{\Delta Q_0}{Q_0}\right)^2 \tag{16}$$

and for the Hall conductance

$$\left(\frac{\Delta\Sigma_H}{\Sigma_P}\right)^2 = \left(\frac{0.85\Delta\langle E \rangle}{\langle E \rangle}\right)^2 + \left(\frac{\Delta\Sigma_P}{\Sigma_P}\right)^2 \tag{17}$$

where $\Delta\langle E \rangle$ and ΔQ_0 correspond to the uncertainties in the average energy and energy flux, respectively.

4. Results

We present two auroral case studies that were part of the PFISR Ion-Neutral Observations in the Thermosphere campaign: 6 November 2012 and 24 November 2012. We present a third, similar event, from the Sondrestrom ISR from 30 November 2013. These auroral events were isolated and not part of a larger geomagnetic storm.

4.1. PFISR 6 November 2012 Event

On 6 November 2012, multiple auroral arcs and diffuse aurora passed through the PFISR field-aligned radar beam between 1200 UT and 1500 UT, as shown in Figure 2. Figures 2a and 2b are, respectively, false-color montages of 557.7 nm and 427.8 nm images that were observed by the all-sky imager collocated with PFISR. The images in this montage were chosen as descriptive examples of the auroral evolution. The white circle corresponds to the PFISR radar beam parallel to the local geomagnetic field, and magnetic north and east are indicated by the N and E labels, respectively (note that the size of the circle is not indicative of the actual size of the radar beam on the sky). At 1212 UT, a zonally extended auroral arc had developed and moved equatorward into the field of view of the radar. This arc brightened and reached maximum visible brightness at

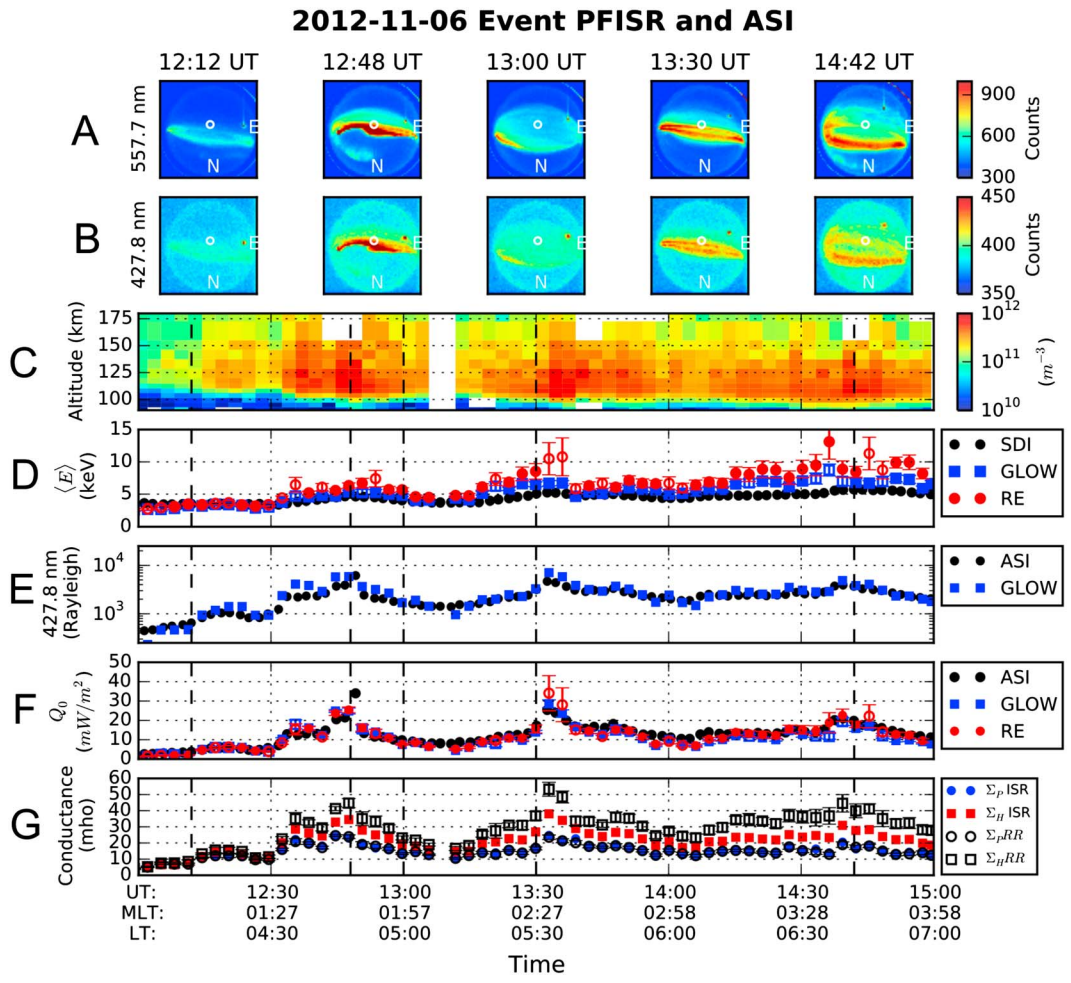

Figure 2. Summary of observations from PFISR on 6 November 2012 from 1200 to 1500 UT. (a and b) The all-sky image montage for 557.7 nm and 427.8 nm, (c) the AC electron number density, (d) the average energy, (e) the 427.8nm emission, (f) the energy flux, and (g) the conductances. White regions in Figure 2c are unsuitable data for this analysis. Parameter estimates from the GLOW and range-energy (RE) model as blue squares and red circles, respectively. All-sky imager (ASI) or SDI observations are shown as black dots. Filled circles or squares are parameter estimates within the 99.99% confidence interval. The Hall and Pedersen conductances are the blue circles and red squares, respectively, and open black circles and squares are the conductances calculated from the Robinson relation. The vertical dotted black lines correspond to 1212, 1248, 1300, 1330, and 1442 UT, respectively.

approximately 1248 UT; immediately afterward an eastward moving ripple passed across the arc. This peak in brightness occurs at both wavelengths. Within minutes of the ripple passage, the arc dissipated into a diffuse background covering most of the sky, which is shown in the 1300 UT panel. By 1330 UT, a new arc had formed and drifted equatorward into the radar field of view. As in the first scenario, the arc brightened, reaching its peak intensity just after 1330 UT as an eastward moving ripple passed across the arc, and then suddenly diffused after the passage of the ripple. At 1400 UT, diffuse aurora remained in the field of view of the radar, even though a stable auroral arc poleward of the radar had developed. Near 1430 UT, an equatorward moving zonally extended but broad auroral arc passed through the radar field of view and again there was subsequent diffusing of the background emission.

Figure 2c shows the AC electron density observed by the ISR as a function of altitude from 80 to 180 km, which is presented for context. Regions of enhanced visible auroral emission clearly correlate with enhancements in the electron number density. White spaces correspond to regions of unsuitable data for this study; within these intervals the noise level was high enough to produce invalid results from the ISR fitting routine. Figure 2d presents the average energy estimates obtained by fitting the forward models to the ISR data and from the SDI observations as described in section 2.2. The 1σ uncertainty estimates

produced by the fitting routine are shown as the error bars. The best fit GLOW and range-energy (RE) model, using a Maxwellian electron flux distribution, are shown as blue squares and red circles, respectively. The average energy derived from the SDI observations are the filled black circles, and the black vertical dashed lines correspond to the time intervals presented in Figures 2a and 2b. Open circles and squares indicate that χ_v^2 of the fit to the data were not within the 99.99% confidence interval; however, we retain all data. The average energy results from the range-energy model, GLOW, and the SDI observations below 5 keV are in very good agreement with each other. For average energies above approximately 5 keV, the SDI underestimates the magnitude relative to the ISR estimates. Higher average energy, corresponding to harder precipitation, is consistent with the observation of a lower altitude edge of the electron number density as shown in Figure 2c between 1230–1300 UT and 1330–1430 UT. The range-energy estimates of the average energy are higher than GLOW between 1315–1345 UT and 1415–1500 UT, over the intervals of predominantly diffuse aurora.

Figure 2e is the 427.8 nm emission obtained from the calibrated all-sky imager versus the 427.8 nm emission predicted by GLOW, for the best fit to the ISR observations. The trend of the calibrated all-sky imager intensity is generally in good agreement with the 427.8 nm emission predicted by GLOW, although there are instances when the magnitude predicted by GLOW is higher than the calibrated imager. Figure 2f follows the results in Figure 2e and shows the energy flux predicted by the all-sky imagers versus the ISR parameter estimates. The energy flux derived from the calibrated all-sky imager using the 427.8 nm emission is shown as black dots, with the blue squares and red circles corresponding to GLOW and range-energy model, respectively. Open squares or circles indicate parameter estimates that do not fall within the 99.99% confidence interval. All-sky imager data, GLOW, and the range-energy model produce consistent results. At some of the lower energy fluxes near 1315 UT and 1400 UT, the ISR estimates are lower than corresponding estimates from the all-sky imager.

Figure 2g presents the Pedersen and Hall conductances calculated from the ISR observations and using the Robinson relation, in equations (14) and (15). The Pedersen and Hall conductances calculated using the AC ISR data are shown as blue filled circles and red filled squares, respectively. The Pedersen and Hall conductances derived from the Robinson relation are shown as open black circles and squares with corresponding error bars calculated using equations (16) and (17), respectively. The Pedersen conductance derived from the ISR observations and the Robinson relation are in excellent agreement with each other, showing values ranging from 10 to 20 mho. The Hall conductances produced by the ISR measurements and results from the Robinson relation show more significant differences, especially in the regions where the average energy exceeds 5 keV. These differences are discussed in section 5.1.

4.2. PFISR 24 November 2012 Event

Figure 3 shows data in a similar format to Figure 2 for an active auroral configuration observed by PFISR on 24 November 2012. Figures 3a and 3b show 557.7 nm and 427.8 nm images, respectively. At approximately 1118 UT, there were several arcs and diffuse aurora that crossed the field-aligned beam between 1100 and 1120 UT. By 1130 UT, diffuse and discrete auroras moved equatorward and evolved as the auroras crossed the field-aligned radar beam. By 1145 UT the arc structure diffused and filled the all-sky imager field of view; this diffuse and pulsating aurora persisted for approximately 15 min.

At 1200 UT, an auroral arc formed poleward of the field-aligned radar beam. This arc brightened and moved equatorward, and an intense eastward moving ripple crossed the field-aligned beam at approximately 1211 UT, which corresponded to the most intense visible emission observed during this event. After the passage of the ripple, the arc rapidly dissipated returning to a diffuse background with some patches of pulsation, similar to the observations from the 6 November 2012 event. These pulsations continued from 1220 UT to 1300 UT, although there was a steady decrease in 557.7 auroral emission. Between 1300 UT and 1315 UT, a weak arc formed over the field-aligned radar beam within the equatorward moving diffuse background. Pulsations returned around 1330 UT and remained until approximately 1350 UT when there was a large visible enhancement over the whole sky; this enhancement peaked at approximately 1354 UT and lasted for approximately 15 min. Between 1400 UT and 1430 UT diffuse and pulsating aurora remained relatively stable over the beam; however, after 1430 UT, as activity decreased the diffuse and pulsating aurora moved poleward out of the radar field of view.

Figure 3d presents the average energy for the interval 1030 UT–1500 UT. From 1030 to 1300 UT, there is good agreement between the ISR estimates of average energy and the SDI estimates for magnitudes < 5 keV. At 1140 UT, there is an abrupt increase in the average energy as the diffuse and discrete aurora move into the

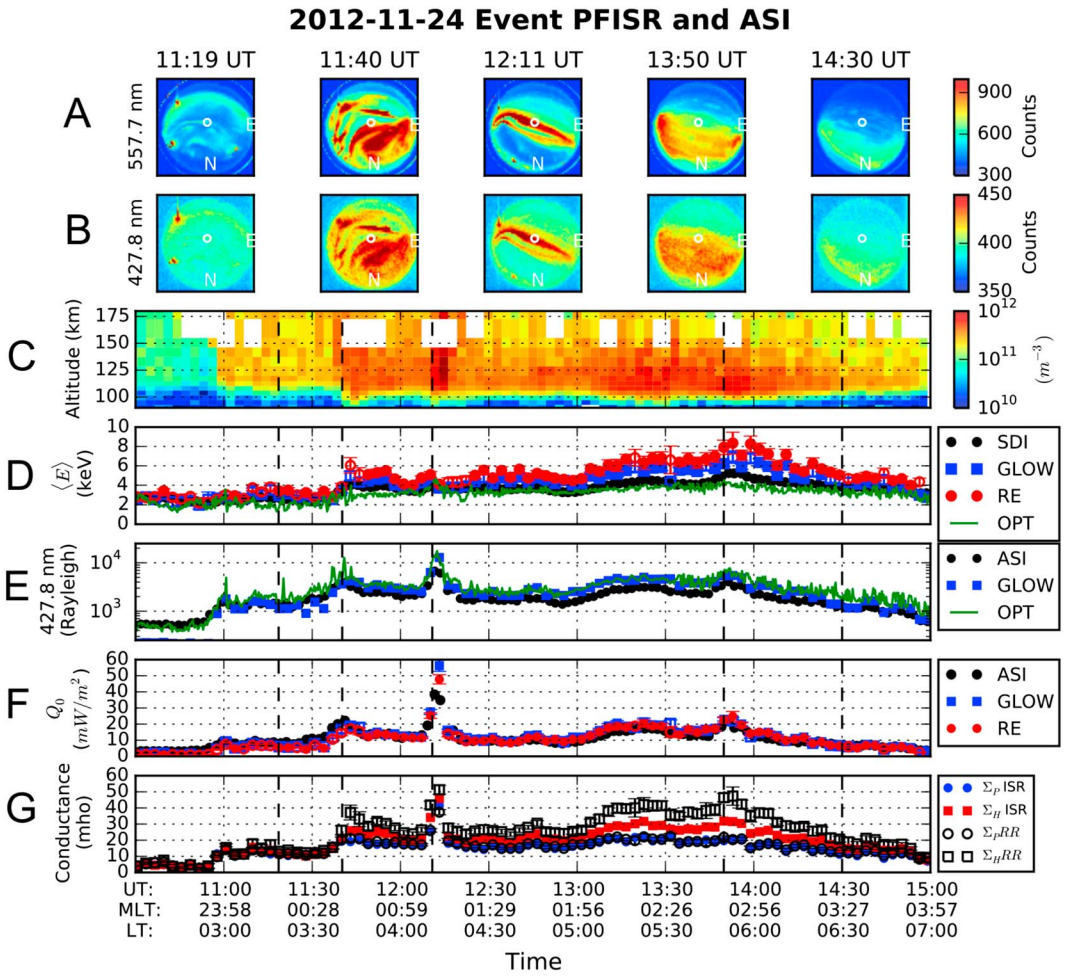

Figure 3. Summary of observations from PFISR on 24 November 2012 from 1030 to 1500 UT. This figure is formatted similar to Figure 2, showing (a and b) the all-sky image montage for 557.7 nm and 427.8 nm, (c) the AC electron number density, (d) the average energy, (e) the 427.8 nm emission, (f) the energy flux, and (g) the conductances. The green curves (labeled as OPT) correspond to observations obtained from The Aerospace Corporation's four-channel optical photometer. The vertical dotted black lines correspond to the times of interest shown in the all-sky montage at 1119 UT, 1140 UT, 1211 UT, 1350 UT, and 1430 UT, respectively.

radar field of view. Between 1140 and 1300 UT the ISR and SDI methods estimate an average energy between 4 and 6 keV. From 1300 UT to 1400 UT, there is an increase in the average energy to 6–8 keV which is consistent with harder precipitation being associated with the diffuse aurora and pulsating aurora within a diffuse background. However, we note that for the 3 min radar integration time, the pulsating aurora is time integrated; the average energy is more representative of the diffuse background versus individual pulsations. In this interval, there is a difference between the average energy estimates from the ISR versus the SDI. The maximum average energy of 8 keV is observed at 1350 UT, which corresponds to the all-sky brightening of the aurora. After 1400 UT, the average energy derived from the ISR begins to decline back to approximately the 2 keV level as the auroral activity diminishes. For the 24 November 2012 event, there are average energy estimates obtained using The Aerospace Corporation's four-channel optical photometer collocated at Poker Flat Research Range (there are no data for the other events). Average energy data are shown in Figure 3d as the green curve with the OPT label. There is good agreement between the SDI observations and the four-channel optical photometer data. The agreement between the SDI and the four-channel optical photometer is especially good in the interval between 1300 and 1430 UT, where the ISR average energy estimate is higher than the estimate produced by the SDI.

Figures 3e and 3f show the 427.8 nm emission and the energy flux, respectively. The 427.8 nm emission predicted by GLOW is, in general, higher relative to observations made by the all-sky imager, similar to the 6

November 2012 event, although the observed 427.8 nm emission and the GLOW 427.8 nm emission estimates track each other very well. However, the 427.8 nm emission data from the four-channel photometer, again shown in green, is in excellent agreement with the predicted GLOW 427.8 nm emission. The agreement is very good between the energy flux estimate using GLOW, the range-energy model, and the all-sky imager observations. At 1215 UT, during the passage of the brightest arc, GLOW and the range-energy model produce estimates near 50 mW/m^2, which are higher than what was produced by the all-sky imager. For the remainder of the event typical energy flux magnitudes were approximately 10 mW/m^2, although during the interval 1300–1400 UT, corresponding to harder precipitation in the diffuse and pulsating regions, the energy flux increases to an average value of approximately 20 mW/m^2. A local maximum in the energy flux of 25 mW/m^2 is observed near 1350 UT, which again corresponds to the all-sky brightness enhancement.

Figure 3g shows the Hall and Pedersen conductances for the 24 November 2012 event. The format is similar to Figure 2g. We again see that the ISR-derived Pedersen conductances versus the Robinson relation are in excellent agreement. The Hall conductance for average energies < 5 keV is generally in good agreement; however, after 1300 UT, in the diffuse aurora, the agreement in the Hall conductance is not as good. The Hall conductance predicted by the Robinson relation is higher during this diffuse aurora interval.

4.3. Sondrestrom 30 November 2013 Event

We present an event from 30 November 2013 from the Sondrestrom ISR between 2130 and 0015 UT, which was the most active time period observed in these case studies. Observations made at Sondrestrom contrast PFISR observations because Sondrestrom routinely is in the polar cap or the cusp, thus potentially sampling different precipitating electron populations [e.g., *Watermann et al.*, 1994; *Kletzing et al.*, 1996]. Figures 4a and 4b begin at approximately 2129 UT, as a multiarc system was observed over the radar field of view, along with intense *E* region ionization. Within minutes after the passage of the arc, there was fading in visible intensity, and other weaker arcs passed through the radar field of view, as shown by Figures 4a and 4b at 2137 UT. The enhanced *E* region ionization, shown in Figure 4c, remained from 2130 to 2200 UT and corresponded to weak arcs and diffuse background emission, with the peak ionization altitude of approximately 125 km.

At 2205 UT, Figures 4a and 4b show a zonally extended arc that was positioned over the radar field of view. This arc developed in the westward part of the field of view and increased in visible intensity as it moved eastward, eventually intersecting the radar field of view at 2205 UT. The arc then moved equatorward during the subsequent minutes after 2205 UT, and the arc structure diminished and diffused rapidly. For the next 30 min weak arcs and diffuse aurora were observed. At approximately 2230 UT, there was a passage of another weaker arc through the field-aligned radar beam. During the next 15 min, the majority of the activity was poleward of the radar field of view. At 2248 UT and 2257 UT, rapidly moving, short-lived arcs caused enhanced *E* region ionization for only a few minutes as shown in Figure 4c. We caution that between 2230 and 2240, there was little auroral activity as indicated by the low electron density in Figure 4c. Parameter estimates within this interval are shown but, due to the lack of backscattered power (low electron number density), may not be accurate.

Figure 4d presents the average energy; there is good agreement between the range-energy model and GLOW over the regions where there was auroral precipitation. In the regions of ionization, for example, between 2130 and 2200 UT, the typical magnitude of the average energy is 2–4 keV. For the arc at 2205 UT, an average energy of 10 keV was observed (from GLOW) which corresponds to the highest average energy observed in the three case studies.

Figure 4e shows strong enhancements at 2129 UT and 2205 UT with energy fluxes of 30 mW/m^2 and 60 mW/m^2, respectively. However, unlike the previous event, the energy flux during the other intervals tends to be lower than the events observed at PFISR. The magnitude of the background energy flux during the 2130 UT–2205 UT interval was > 10 mW/m^2, whereas in the 6 November 2012 and 24 November 2012, the energy flux was < 10 mW/m^2. The characteristic energy and energy flux suggest that these aurora were caused by harder precipitation and weaker energy fluxes.

We see the best agreement between the conductance observed by the ISR and the conductances derived by the Robinson relation for this event. Figure 4e shows that the Hall and Pedersen conductances agree very well with each other and the value derived by the ISR. However, at 2205 UT the largest departure in the Hall conductance between the two methods occurred; the ISR observed approximately 40 mho, whereas the Robinson relation estimated approximately 80 mho. At the latter enhancements, at 2248 UT and 2257 UT,

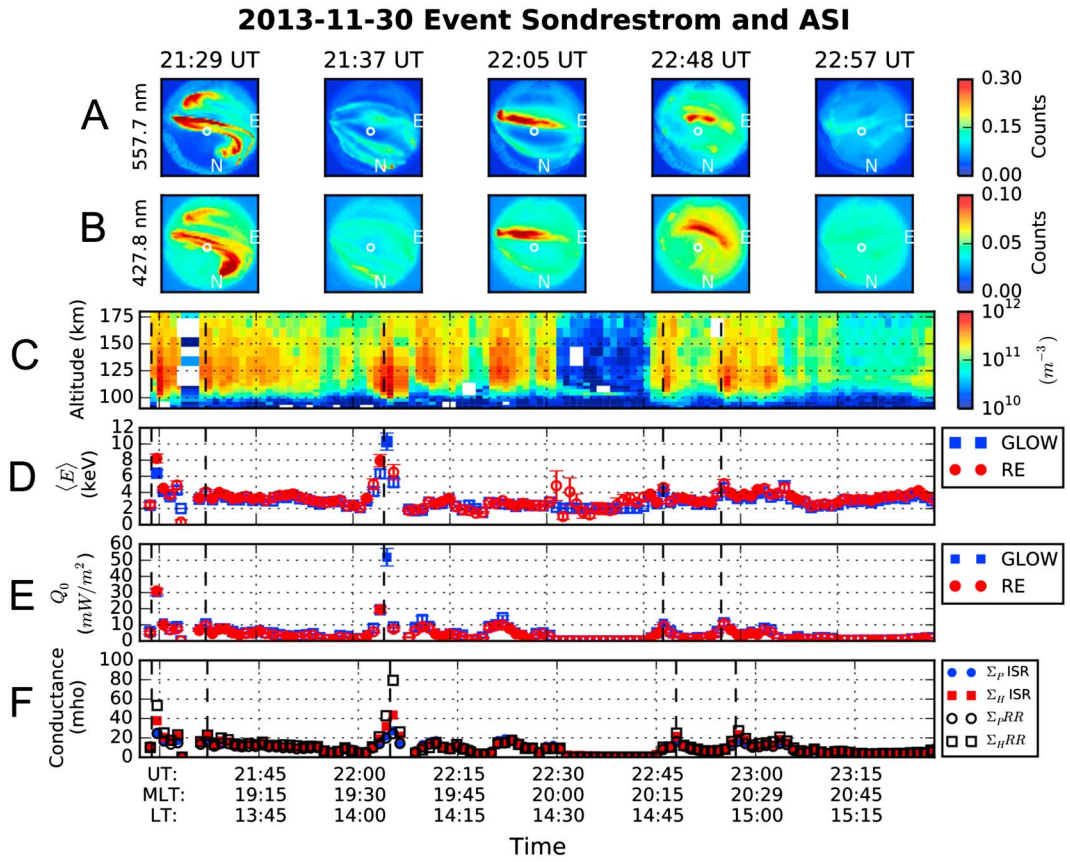

Figure 4. Observations from Sondrestrom on 30 November 2013 from 2130 to 2300 UT. This figure is formatted similar to Figure 2, showing (a and b) the all-sky image montage for 557.7nm and 427.8nm, (c) the AC electron number density, (d) the average energy, (e) the energy flux, and (f) the conductances. The vertical dotted black lines correspond to the times of interest shown in the all-sky montage at 2129 UT, 2137 UT, 2205 UT, 2248 UT, and 2257 UT, respectively.

there is a slight difference between the ISR observed Hall conductance and the Hall conductance calculated using the Robinson relation.

5. Discussion

We find similarity between these three auroral events, despite being within different regions of geospace and various activity levels. The average energy estimated by the ISR in the events ranged from 2 to 10 keV, with harder precipitation being associated with diffuse aurora and pulsating aurora in diffuse background. For the very active arc, such as the Sondrestrom 30 November 2013 event at 22:05 UT, there was an isolated instance where the average energy was 10 keV associated with this active arc. The energy fluxes observed over the discrete and diffuse (including pulsating) aurora ranged from 10 to 60 mW/m^2. Finally, the Pedersen and Hall conductances derived from the ISR (not using the Robinson relation) ranged at 10–25 mho and 10–40 mho, respectively. These results are consistent with previous observations and climatological studies of the energy flux, characteristic (average) energy, and conductance over the auroral zone [*Wallis and Budzinski*, 1981; *Harel et al.*, 1981; *Spiro et al.*, 1982; *Hardy et al.*, 1987; *Hecht et al.*, 2006; *Lanchester et al.*, 2009; *Lanchester and Gustavsson*, 2012; *Feldstein et al.*, 2014].

For the SDI and ISR methods, the time integration of the data leads to a selection bias toward precipitation that remains spatially stable over the field-aligned radar beam. Although there are signatures of transient intense precipitation that have been presented, it is more likely that the 2–3 min integration along the radar beam is sensitive to aurora that remains spatially stable over the field-aligned beam, whether that aurora is diffuse or discrete. The properties of diffuse auroral precipitation over the field-aligned beam are likely to be more accurately estimated using these methods. Thus, we would expect our estimates to be more consistent with diffuse aurora parameters, unless an arc remains stable over the field-aligned radar beam.

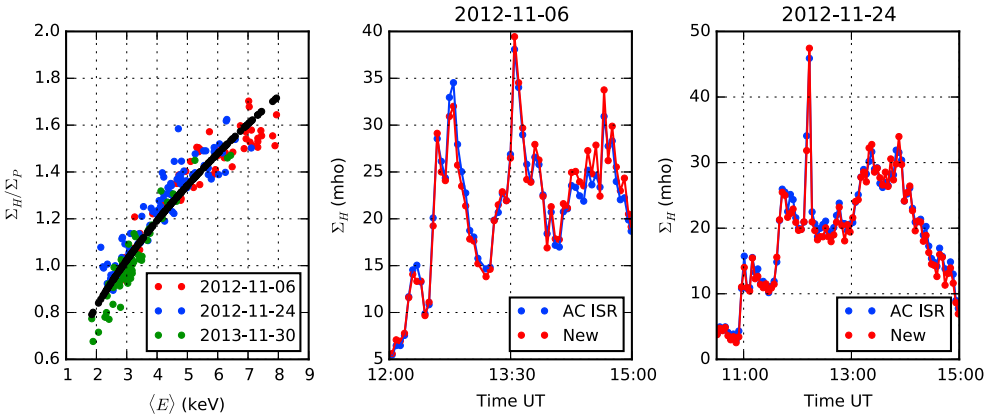

Figure 5. A comparison of the Hall conductance determined by the ISR versus the Hall conductance determined using the formulas by *Robinson et al.* [1987]. (left) Data from the 6 November 2012, 24 November 2012, and 30 November 2013 as red, blue, and green dots, respectively. The fit is shown as the black dots. (middle) The updated Robinson relation is applied, labeled as New in the legend, using the GLOW fit characteristic energy in red and the ISR calculated Hall conductance in blue for the 6 November 2012 event. (right) The updated empirical model for the 24 November 2012 event.

Dahlgren et al. [2015] recently presented observational evidence suggesting a further ambiguity, that there may be multiple electron populations that are present along a given magnetic flux tube, each with its own morphology and flow across the field of view. For the case study by *Dahlgren et al.* [2015], lower energy auroral filaments were found within larger pulsating patches. It is likely if our configuration made similar observations the parameter estimates would be more consistent with time-averaged pulsating patches versus the simultaneously observed low energy precipitation.

5.1. Characteristic Energy and Conductance Estimates

There is nearly a factor of 2 difference between the PFISR derived Hall conductance versus the Hall conductance derived from the Robinson relation in Figures 2 and 3, whereas the Pedersen conductance determined by both methods is consistent. It is a commonly observed feature that the ratio of the Hall to Pedersen conductances is greater than unity over aurora, which indicates the presence of energetic electron precipitation [*Brekke et al.*, 1989]. We calculated the Hall and Pedersen conductances from the ISR observations and have obtained estimates of the energy flux and average energy; thus, we can obtain an updated relation that connects these parameters. If we assume that the empirical form of equation (15) is valid,

$$\frac{\Sigma_H}{\Sigma_P} = A\langle E \rangle^{\alpha} \tag{18}$$

then we can determine A and the power law index α using a linear least squares fit after taking the logarithm of equation (18). Figure 5 (left) shows the results of fitting for A and α. The red dots correspond to the data points between 12:00 and 15:00 UT for the PFISR 6 November 2012 event, the blue dots correspond to the PFISR 24 November 2012 event between 10:30 UT and 15:00 UT, and the green dots correspond to the Sondrestrom 30 November 2013 event from 21:30 to 22:00 (we applied a 5 mho threshold). The black curve corresponds to the fit of these data, with $A = 0.57$ and $\alpha = 0.53$. The 30 November 2013 event forms the majority of the data at the lower magnitudes of average energy and ratio of Σ_H/Σ_P, whereas the 6 November 2012 event forms the region of the highest magnitude of average energy and ratio of Σ_H/Σ_P.

Figures 5 (middle) and 5 (right) show the Hall conductance estimated by the ISR in blue versus the new relation (labeled as NEW) in red for the 6 November 2012 and 24 November 2012 event, respectively. We do not show the 30 November 2013 event, since the estimate of the Hall and Pedersen conductances is in good agreement between the ISR and Robinson relation. The agreement is very good in both events, and this relation does appear to match the data much better than the relation in *Robinson et al.* [1987]; however, the updated relation is valid for average energies < 8 keV. One of the factors that could account for the difference in the two relations has to do with the choice of neutral model. *Robinson et al.* [1987] and *Vickrey et al.* [1981] used the 1000° neutral atmosphere model in *Banks and Kockarts* [1973], whereas the model we use is the MSIS00 model. Changes in mass density will impact the effectiveness of the precipitating electrons and could shift the peak with respect to altitude, thus changing the magnitude of the Hall conductance.

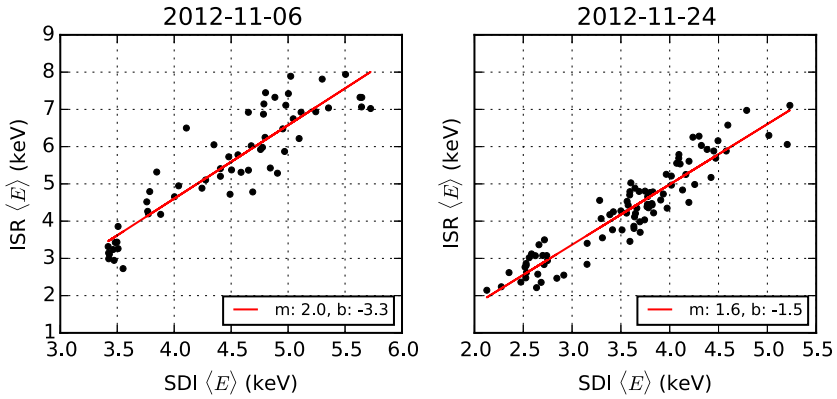

Figure 6. Hodograms of the average energy derived from the SDI versus the characteristic energy estimate from the ISR for the (left) 6 November 2012 and (right) 24 November 2012 events. The slope of the curve and the intercept are indicated in the legend as *m* and *b*, respectively.

The average energy estimate > 5 keV determined by the SDI was lower versus the ISR derived characteristic energy estimate by approximately a factor of 2. Figure 6 shows the SDI versus ISR characteristic energy for the 6 November 2012 and 24 November 2012 events, respectively. It is clear that the characteristic energy estimates from the SDI and ISR are linear. To quantify this difference, we used a least squares linear fit and found a slope of 2.0±0.1 and 1.6±0.1 for the 6 November 2012 and 24 November 2012 events, respectively. For the 6 November 2012 event and the 24 November 2012 event there is a clustering of data points near ≈ 3.5 keV (SDI) and 2.5 keV (SDI), respectively. These correspond to the region where the agreement between the SDI estimates and the ISR estimates are very good. At higher average energies there is a larger difference, and this spread is particularly significant for the 6 November 2012 event.

One of the sources of uncertainty when using the SDI technique is determining the characteristic (average) energy from the neutral atmosphere model. To simulate the effect an enhanced neutral atmosphere has on the estimation of the characteristic energy, we examined the neutral temperature profile. This simulation does not take into account the effect of convolving optical emission which has been included in the data presented in Figures 2 and 3. Figure 7 presents the results from a simplified calculation, which pertain to the previous results. Figure 7 (left) shows the MSIS neutral temperature (T_n) versus altitude, for altitudes ranging from 100 to 150 km. The black curve in Figure 7 (left) corresponds to $F_{10.7} = 15$ and AP index = 125; these were the MSIS parameters observed during the interval 1200–1500 UT. A significant point is that the temperature profiles converge near 102 km to approximately 200K.

Figure 7 (middle) is the peak altitude emission for the 557.7 nm emission calculated using GLOW as a function of characteristic energy, for an input Maxwellian flux distribution with an energy flux of 10 mW/m^2. For characteristic energies < 1 keV (average energy < 2 keV), the altitude of peak emission is highly sensitive to the characteristic energy for this instance of the neutral atmosphere. Between 1 and 3 keV (average energy 2–6 keV), the response is nonlinear, and for > 3 keV (average energy > 6 keV), the response is linear and nearly flat with characteristic energy. By interpolating with respect to altitude the results from Figures 7 (left) and 7 (middle), it is possible to generate a response curve for the characteristic energy given an observed neutral temperature measurement, as shown in Figure 7 (right). In Figure 7 (middle), the neutral temperature has a strong linear response between 800 and 400 K, corresponding to characteristic energies between 0.5 and 1 keV (average energy 1–2 keV). From 400 to 230 K the response is nonlinear for characteristic energies between 1 and 3 keV (average energy 2–6 keV) and > 3 keV (average energy > 6 keV); the response converges to approximately 200 K. The response above 3 keV is consistent with Figure 7 (left), as the neutral temperatures converge to 200 K.

Figure 7 (right) shows an important point regarding electron fluxes with high characteristic energies: the asymptotic response implies that this method becomes less sensitive at higher characteristic energies. Figure 7 (right) shows neutral temperature convergence above a characteristic energy of 4 keV to approximately 200K, and the response curve is nearly flat, implying that a slight difference in a neutral temperature observation will produce a significant change in the characteristic energy estimate. We find that our results are consistent with results in *Hecht et al.* [2006]. This simplistic approach did not take into account the proper

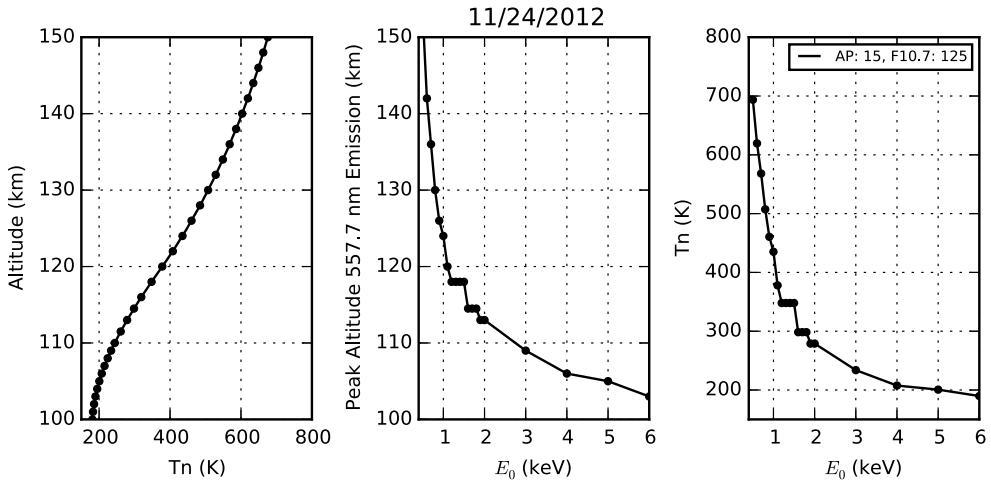

Figure 7. Results from a simplified calculation to quantify the Scanning Doppler Imager measurement of characteristic energy for the 24 November 2012 event. (left) MSIS profiles of the neutral temperature (T_n) as a function of altitude for various $F_{10.7}$ and ""AP values, shown in the legend. (middle) The peak emission altitude for the 557.7 nm emission line as a function of characteristic energy. We assumed that the flux distribution was a Maxwellian with a constant energy flux of 10 mW/m^2. (right) Interpolated response curves of neutral temperature versus characteristic energy. The response shows that there is a strong linear response for characteristic energies < 1 keV (average energy < 2 keV), a nonlinear response between 1 and 3 keV (average energy 2–6 keV), and a nearly flat response for > 3 keV (average energy > 6 keV).

optical convolution of the SDI data; however, a similar response curve shows a flattening in the response as the characteristic energy approaches 10 keV (this is to be presented in an upcoming paper, along with an in-depth discussion of this technique). This could partially explain why the observed average energies for the 6 November 2012 and 24 November 2012 showed a difference in average energies > 5 keV.

A second related point is that the SDI must be capable of resolving low temperature measurements that correspond to high characteristic energy. This can be challenging as the thermal broadening of the observed spectral width decreases and pushes the sensitivity of the instrument. For the case studies presented, the minimum temperature observed for the 24 November 2012 event was near 300 K, which suggests a maximum characteristic energy of 2 keV (average energy 4 keV), using the simplistic analysis.

5.2. Incident Electron Flux Distribution

For GLOW and the range-energy model, the electron flux distribution was assumed to be a Maxwellian. The regularization techniques [e.g., *Brekke et al.*, 1989; *Kirkwood*, 1988; *Semeter and Kamalabadi*, 2005] removed this assumption and obtained an estimate of the electron flux by inverting the ISR data; thus, these techniques are more general. However, there are a few important points to be made regarding the validity of the method we put forth. First, both the range-energy model or GLOW can ingest an arbitrary electron flux distribution, provided that the number flux can be numerically integrated to produce a finite value. It is possible to incorporate a double Maxwellian, kappa, or similar distribution [e.g., *Fang et al.*, 2010]. We recognize that our model effectively smooths over possible small scale variations in the electron number density that could be caused by localized ionization enhancements. Our method does obtain the general character of the ionization profile with respect to altitude, even if it is not able to capture every excursion in the electron density observed by the ISR. Second, the best fits of the forward model to the ISR data were within the data uncertainties. There is one notable exception: below 100 km the electron number density produced by the forward model tended to decay more rapidly with altitude versus the ISR observation. Those data did not in general fit within the error estimate provided by the ISR observations. This may suggest, in addition to an improper electron distribution, that the chemistry model in the lower *E* region and upper *D* region requires some modification; however, this is outside of the scope of this paper. Third, we found that for the majority of the fits over visible aurora the Maxwellian flux distribution does a sufficient job reproducing the ionization that was observed by the ISR. In situations where there was a clear single peak, we were able to fit the ionization profile to the peak ionization. This point suggests that a Maxwellian-type distribution is a very good, smooth, approximation of the true electron distribution that we are estimating.

6. Conclusion

We present results from three case studies of the energy flux, average energy, and conductance that were produced by directly fitting results from an electron transport code, GLOW, to alternating code ISR electron number density observations. The case studies corresponded to auroral configurations observed along the direction of the geomagnetic field. These fits were also found to be in good agreement with an experimentally derived range-energy relation first described in *Rees* [1963] and more recently revisited in *Semeter and Kamalabadi* [2005]. A Maxwellian flux distribution describing the precipitating electrons is found to be a sufficient description of the precipitating electron flux that generates enhanced *E* region ionization. We found typical energy fluxes between 10 and 30 mW/m^2, with the strongest energy flux of 60 mW/m^2 being observed at a time when an intense arc was moving over the radar field of view. The estimates of average energy range from 2 to 8 keV, with harder electron precipitation being observed during diffuse and pulsating aurora. These results are consistent with previous studies of precipitating auroral electrons. We also noted some difference in the magnitudes of the energy flux and average energy between observations at PFISR versus the Sondrestrom ISR, which could indicate probing different electron population sources and acceleration processes. By directly fitting a forward electron transport model to the ISR data, we are able to obtain estimates for volume emission rates, the upward and downward directed electron flux as a function of altitude and energy, and other parameters calculated internally in the transport model.

We find that the scanning Doppler imager (SDI) Fabry-Perot interferometer observations can be used to produce estimates of the average energy. We find that for average energies < 5.0 keV, the ISR and SDI produce consistent results but for average energies > 5.0 keV the SDI underestimates the magnitude relative to the ISR. A simplistic analysis was performed on the technique to determine the characteristic energy of a Maxwellian distribution function using the neutral temperature measurements, and it was found that this technique is most sensitive for electrons with characteristic energies < 4 keV. However, we also found that as the characteristic energy approaches 4–5 keV, the response becomes nearly flat, where small changes in the observed neutral temperature correspond to a significant change in the characteristic energy estimate, causing a potential ambiguity in the characteristic (average) energy estimate.

We calculated the Hall and Pedersen conductances using ISR observations and compared our results with the relation by *Robinson et al.* [1987]. The Pedersen conductance calculated directly from the ISR observations was in good agreement with the Pedersen conductance determined using the relation by *Robinson et al.* [1987] when the energy flux and characteristic energy determined by the ISR were used. However, the Hall conductance between the ISR and Robinson relation were different by approximately a factor of 2 in both events. We took data from the three events and fit to determine an updated Robinson relation for this event and found that $\Sigma_H/\Sigma_P = 0.57\langle E\rangle^{0.53}$ in this case, where $\langle E\rangle$ is the average energy for the Maxwellian distribution ($\langle E\rangle = 2E_0$). These results are limited to similar events to the three case studies used that were chosen during moderate nonsubstorm expansion auroral activity with 557.7 nm intensities greater than 1kR. This relation produces better agreement when using the characteristic energy and energy flux (implicitly when solving for the Pedersen conductance, Σ_P, in equation (14)). We find typical values for the Pedersen conductance of 10–25 mho and for the Hall conductance between 15 and 30 mho, which are consistent with previous studies.

Acknowledgments

This work was supported by National Science Foundation (NSF) grant AGS-1133009, AGS-1242913, and NSF PLR-1445376 to SRI International. Analysis at the University of Alaska Fairbanks Geophysical Institute was funded by NASA grant NNX10AL20G and by NSF grant AGS-1242913. Analysis at the National Center for Atmospheric Research (NCAR) was funded by NASA grant NNX13AE15G. NCAR is supported by the National Science Foundation. Support for this work is also provided by The Aerospace Corporation's SERPA program. Incoherent scatter radar data for these events can be found at http://isr.sri.com/madrigal/ or http://www.amisr.com. All-sky imager data can be found at http://optics.gi.alaska.edu/optics/. Data will be made available by contacting the first author.

Michael Liemohn thanks two reviewers for their assistance in evaluating this paper.

References

Anderson, C., M. J. Kosch, M. J. Nicolls, and M. Conde (2013), Ion-neutral coupling in Earth's thermosphere, estimated from concurrent radar and optical observations above Alaska, *J. Atmos. Sol. Terr. Phys.*, *105*, 313–324, doi:10.1016/j.jastp.2013.04.005.

Banks, P. M., and G. Kockarts (1973), *Aeronomy*, Academic Press, Univ. of Calif.

Banks, P. M., C. R. Chappell, and A. F. Nagy (1974), A new model for the interaction of auroral electrons with the atmosphere: Spectral degradation, backscatter, optical emission, and ionization, *J. Geophys. Res.*, *79*, 1459–1470, doi:10.1029/JA079i010p01459.

Barrett, J. L., and P. B. Hays (1976), Spatial distribution of energy deposited in nitrogen by electrons, *J. Chem. Phys.*, *64*, 743–750, doi:10.1063/1.432221.

Basu, B., J. R. Jasperse, D. J. Strickland, and R. E. Daniell Jr. (1993), Transport-theoretic model for the electron-proton-hydrogen atom aurora. 1: Theory, *J. Geophys. Res.*, *98*, 21,517–21,532, doi:10.1029/93JA01646.

Bevington, P., and D. Robinson (2003), *Data Reduction and Error Analysis for the Physical Sciences*, McGraw-Hill, Univ. of Michigan.

Boström, R. (1964), A model of the auroral electrojects, *J. Geophys. Res.*, *69*, 4983–4999, doi:10.1029/JZ069i023p04983.

Brekke, A., C. Hall, and T. L. Hansen (1989), Auroral ionospheric conductances during disturbed conditions, *Ann. Geophys.*, *7*, 269–280.

Butler, T. W., J. Semeter, C. J. Heinselman, and M. J. Nicolls (2010), Imaging *F* region drifts using monostatic phased-array incoherent scatter radar, *Radio Sci.*, *45*, RS5013, doi:10.1029/2010RS004364.

Chamberlain, J. W. (1961), *Physics of the Aurora and Airglow*, AGU, Washington, D. C.

Conde, M., and R. W. Smith (1995), Mapping thermospheric winds in the auroral zone, *Geophys. Res. Lett.*, *22*, 3019–3022, doi:10.1029/95GL02437.

Conde, M., and R. W. Smith (1997), Phase compensation of a separation scanned, all-sky imaging Fabry Perot spectrometer for auroral studies, *Appl. Opt.*, *36*, 5441–5450, doi:10.1364/AO.36.005441.

Dahlgren, H., N. Ivchenko, B. S. Lanchester, J. Sullivan, D. Whiter, G. Marklund, and A. Strømme (2008), Using spectral characteristics to interpret auroral imaging in the 731.9 nm O^+ line, *Ann. Geophys.*, *26*, 1905–1917, doi:10.5194/angeo-26-1905-2008.

Dahlgren, H., B. Gustavsson, B. S. Lanchester, N. Ivchenko, U. Brändström, D. K. Whiter, T. Sergienko, I. Sandahl, and G. Marklund (2011), Energy and flux variations across thin auroral arcs, *Ann. Geophys.*, *29*, 1699–1712, doi:10.5194/angeo-29-1699-2011.

Dahlgren, H., B. S. Lanchester, and N. Ivchenko (2015), Coexisting structures from high- and low-energy precipitation in fine-scale aurora, *Geophys. Res. Lett.*, *42*(5), 1290–1296, doi:10.1002/2015GL063173.

Dalgarno, A., I. D. Latimer, and J. W. McConkey (1965), Corpuscular bombardment and N_2^+ radiation, *Planet. Space Sci.*, *13*, 1008–1009, doi:10.1016/0032-0633(65)90160-1.

Doe, R. A., J. D. Kelly, D. Lummerzheim, G. K. Parks, M. J. Brittnacher, G. A. Germany, and J. Spann (1997), Initial comparison of POLAR UVI and Sondrestrom IS radar estimates for auroral electron energy flux, *Geophys. Res. Lett.*, *24*, 999–1002, doi:10.1029/97GL00376.

Evans, D. S., N. C. Maynard, J. Troim, T. Jacobsen, and A. Egeland (1977), Auroral vector electric field and particle comparisons. II—Electrodynamics of an arc, *J. Geophys. Res.*, *82*, 2235–2249, doi:10.1029/JA082i016p02235.

Fang, X., C. E. Randall, D. Lummerzheim, W. Wang, G. Lu, S. C. Solomon, and R. A. Frahm (2010), Parameterization of monoenergetic electron impact ionization, *Geophys. Res. Lett.*, *37*, L22106, doi:10.1029/2010GL045406.

Feldstein, Y. I., V. G. Vorobjev, V. L. Zverev, and M. Förster (2014), Investigations of the auroral luminosity distribution and the dynamics of discrete auroral forms in a historical retrospective, *Hist. Geo Space. Sci.*, *5*, 81–134, doi:10.5194/hgss-5-81-2014.

Gattinger, R. L., A. V. Jones, J. H. Hecht, D. J. Strickland, and J. Kelley (1991), Comparison of ground-based optical observations of N_2 second positive to $N_2^{(+)}$ first negative emission ratios with electron precipitation energies inferred from the Sondre Stromfjord radar, *J. Geophys. Res.*, *96*, 11,341–11,351, doi:10.1029/91JA01015.

Grün, A. E. (1957), Lumineszenz-photometrische Messunen der Energieabsorption im Strahlungsfeld von Electronenquellen. Eindimensionaler Fall in Luft, *Z. Naturforsch. Teil A*, *12*, 89–95, doi:10.1515/zna-1957-0201.

Hardy, D. A., M. S. Gussenhoven, R. Raistrick, and W. J. McNeil (1987), Statistical and functional representations of the pattern of auroral energy flux, number flux, and conductivity, *J. Geophys. Res.*, *92*, 12,275–12,294, doi:10.1029/JA092iA11p12275.

Harel, M., R. A. Wolf, P. H. Reiff, R. W. Spiro, W. J. Burke, F. J. Rich, and M. Smiddy (1981), Quantitative simulation of a magnetospheric substorm. I—Model logic and overview, *J. Geophys. Res.*, *86*, 2217–2241, doi:10.1029/JA086iA04p02217.

Hecht, J. H., A. B. Christensen, D. J. Strickland, and R. R. Meier (1989), Deducing composition and incident electron spectra from ground-based auroral optical measurements: Variations in oxygen density, *J. Geophys. Res.*, *94*, 13,553–13,563, doi:10.1029/JA094iA10p13553.

Hecht, J. H., D. J. Strickland, and M. G. Conde (2006), The application of ground-based optical techniques for inferring electron energy deposition and composition change during auroral precipitation events, *J. Atmos. Sol. Terr. Phys.*, *68*, 1502–1519, doi:10.1016/j.jastp.2005.06.022.

Heinselman, C. J., and M. J. Nicolls (2008), A Bayesian approach to electric field and *E*-region neutral wind estimation with the Poker Flat Advanced Modular Incoherent Scatter Radar, *Radio Sci.*, *43*, RS5013, doi:10.1029/2007RS003805.

Holmes, J. M., M. Conde, C. Deehr, and D. Lummerzheim (2005), Morphology of evening sector aurorae in λ557.7-nm Doppler temperatures, *Geophys. Res. Lett.*, *32*, L02103, doi:10.1029/2004GL021553.

Jones, S. L., M. R. Lessard, P. A. Fernandes, D. Lummerzheim, J. L. Semeter, C. J. Heinselman, K. A. Lynch, R. G. Michell, P. M. Kintner, H. C. Stenbaek-Nielsen, and K. Asamura (2009), Pfisr and ropa observations of pulsating aurora, *J. Atmos Sol. Terr. Phys.*, *71*(6), 708–716, doi:10.1016/j.jastp.2008.10.004.

Jursa, A. S., et al. (1985), *Handbook of Geophysics and the Space Environment*, Air Force Geophysics Laboratory Hanscom, San Francisco, Calif.

Kaeppler, S. R. (2013), A rocket-borne investigation of auroral electrodynamics within the auroral-ionosphere, PhD thesis, Univ. of Iowa, Iowa.

Kaeppler, S. R., M. J. Nicolls, A. Stromme, C. A. Kletzing, and S. R. Bounds (2014), Observations in the E region ionosphere of kappa distribution functions associated with precipitating auroral electrons and discrete aurorae, *J. Geophys. Res. Space Physics*, *119*, 10,164–10,183, doi:10.1002/2014JA020356.

Kasting, J. F., and P. B. Hays (1977), A comparison between N2/+/ 4278-A emission and electron flux in the auroral zone, *J. Geophys. Res.*, *82*, 3319–3323, doi:10.1029/JA082i022p03319.

Kelly, J. D., and C. J. Heinselman (2009), Initial results from Poker Flat Incoherent Scatter Radar (PFISR), *J. Atmos. Sol. Terr. Phys.*, *71*(6), 635, doi:10.1016/j.jastp.2009.01.009.

Kirkwood, S. (1988), SPECTRUM: A computer algorithm to derive the flux-energy spectrum of precipitating particles from EISCAT electron density profiles, Tech. Rep., National Aeronautics and Space Administration, Kiruna, Sweden.

Kivelson, M. G., and C. T. Russell (1995), *Introduction to Space Physics*, Cambridge Univ. Press, Cambridge, U. K.

Kletzing, C. A., G. Berg, M. C. Kelley, F. Primdahl, and R. B. Torbert (1996), The electrical and precipitation characteristics of morning sector Sun-aligned auroral arcs, *J. Geophys. Res.*, *101*, 17,175–17,190, doi:10.1029/96JA00294.

Kletzing, C. A., F. S. Mozer, and R. B. Torbert (1998), Electron temperature and density at high latitude, *J. Geophys. Res.*, *103*, 14,837–14,846, doi:10.1029/98JA00962.

Lanchester, B., and B. Gustavsson (2012), Imaging of aurora to estimate the energy and flux of electron precipitation, in *Auroral Phenomenology and Magnetospheric Processes: Earth and Other Planets,* vol. 197, edited by A. Keiling et al., pp. 171–182, AGU, Washington, D. C., doi:10.1029/2011GM001161

Lanchester, B. S., M. H. Rees, D. Lummerzheim, A. Otto, H. U. Frey, and K. U. Kaila (1997), Large fluxes of auroral electrons in filaments of 100 m width, *J. Geophys. Res.*, *102*, 9741–9748, doi:10.1029/97JA00231.

Lanchester, B. S., M. Ashrafi, and N. Ivchenko (2009), Simultaneous imaging of aurora on small scale in OI (777.4 nm) and $N_2$1P to estimate energy and flux of precipitation, *Ann. Geophys.*, *27*, 2881–2891, doi:10.5194/angeo-27-2881-2009.

Lummerzheim, D., and J. Lilensten (1994), Electron transport and energy degradation in the ionosphere: Evaluation of the numerical solution, comparison with laboratory experiments and auroral observations, *Ann. Geophys.*, *12*, 1039–1051, doi:10.1007/s00585-994-1039-7.

Nagy, A. F., and P. M. Banks (1970), Photoelectron fluxes in the ionosphere, *J. Geophys. Res.*, *75*, 6260–6270, doi:10.1029/JA075i031p06260.

Nicolls, M. J., R. Cosgrove, and H. Bahcivan (2014), Estimating the vector electric field using monostatic, multibeam incoherent scatter radar measurements, *Radio Sci.*, *49*, 1124–1139, doi:10.1002/2014RS005519.

Ogasawara, K., K. Asamura, T. Takashima, Y. Saito, and T. Mukai (2006), Rocket observation of energetic electrons in the low-altitude auroral ionosphere during the DELTA campaign, *Earth Planets Space*, *58*, 1155–1163.

Picone, J. M., A. E. Hedin, D. P. Drob, and A. C. Aikin (2002), NRLMSISE-00 empirical model of the atmosphere: Statistical comparisons and scientific issues, *J. Geophys. Res.*, *107*, 1468, doi:10.1029/2002JA009430.

Press, W., S. Teukolsky, W. Vetterling, and B. Flannery (2007), *Numerical Recipes 3rd Edition: The Art of Scientific Computing*, Numerical Recipes: The Art of Scientific Computing, Cambridge Univ. Press, New York.

Rees, M. H. (1963), Auroral ionization and excitation by incident energetic electrons, *Planet. Space Sci.*, *11*, 1209–1218, doi:10.1016/0032-0633(63)90252-6.

Rees, M. H. (1989), *Physics and Chemistry of the Upper Atmosphere*, Cambridge Univ. Press, Cambridge, U. K.

Rees, M. H., and D. Luckey (1974), Auroral electron energy derived from ratio of spectroscopic emissions. I—Model computations, *J. Geophys. Res.*, *79*, 5181–5186, doi:10.1029/JA079i034p05181.

Reiff, P. H. (1984), Models of auroral-zone conductances, in *Magnetospheric Currents*, edited by T. A. Potemra, pp. 180–191, AGU, Washington, D. C.

Robinson, R. M., R. R. Vondrak, K. Miller, T. Dabbs, and D. Hardy (1987), On calculating ionospheric conductances from the flux and energy of precipitating electrons, *J. Geophys. Res.*, *92*, 2565–2569, doi:10.1029/JA092iA03p02565.

Schunk, R. W., and A. F. Nagy (2004), *Ionospheres: Physics, Plasma Physics and Chemistry*, Cambridge Univ. Press, Cambridge, U. K.

Semeter, J., and F. Kamalabadi (2005), Determination of primary electron spectra from incoherent scatter radar measurements of the auroral *E* region, *Radio Sci.*, *40*, RS2006, doi:10.1029/2004RS003042.

Semeter, J., and M. Zettergren (2014), Model-based inversion of auroral processes, in *Modeling the Ionosphere-Thermosphere System*, pp. 309–321, John Wiley, Chichester, U. K., doi:10.1002/9781118704417.ch25

Semeter, J., D. Lummerzheim, and G. Haerendel (2001), Simultaneous multispectral imaging of the discrete aurora, *J. Atmos. Sol. Terr. Phys.*, *63*, 1981–1992, doi:10.1016/S1364-6826(01)00074-8.

Semeter, J., T. Butler, C. Heinselman, M. Nicolls, J. Kelly, and D. Hampton (2009), Volumetric imaging of the auroral ionosphere: Initial results from PFISR, *J. Atmos. Sol. Terr. Phys.*, *71*, 738–743, doi:10.1016/j.jastp.2008.08.014.

Simon Wedlund, C., H. Lamy, B. Gustavsson, T. Sergienko, and U. Brändström (2013), Estimating energy spectra of electron precipitation above auroral arcs from ground-based observations with radar and optics, *J. Geophys. Res. Space Physics*, *118*, 3672–3691, doi:10.1002/jgra.50347.

Solomon, S. C. (2001), Auroral particle transport using Monte Carlo and hybrid methods, *J. Geophys. Res.*, *106*, 107–116, doi:10.1029/2000JA002011.

Solomon, S. C., P. B. Hays, and V. J. Abreu (1988), The auroral 6300 A emission—Observations and modeling, *J. Geophys. Res.*, *93*, 9867–9882, doi:10.1029/JA093iA09p09867.

Spiro, R. W., P. H. Reiff, and L. J. Maher Jr. (1982), Precipitating electron energy flux and auroral zone conductances—An empirical model, *J. Geophys. Res.*, *87*, 8215–8227, doi:10.1029/JA087iA10p08215.

Strickland, D. J., R. R. Meier, J. H. Hecht, and A. B. Christensen (1989), Deducing composition and incident electron spectra from ground-based auroral optical measurements. I—Theory and model results. II—A study of auroral red line processes. III—Variations in oxygen density, *J. Geophys. Res.*, *94*, 13,527–13,539, doi:10.1029/JA094iA10p13527.

Strickland, D. J., R. E. Daniell Jr., J. R. Jasperse, and B. Basu (1993), Transport-theoretic model for the electron-proton-hydrogen atom aurora. 2: Model results, *J. Geophys. Res.*, *98*, 21,533–21,548, doi:10.1029/93JA01645.

Strickland, D. J., J. H. Hecht, A. B. Christensen, and J. Kelly (1994), Relationship between energy flux Q and mean energy $\langle E \rangle$ of auroral electron spectra based on radar data from the 1987 CEDAR Campaign at Sondre Stromfjord, Greenland, *J. Geophys. Res.*, *99*, 19,467–19,473, doi:10.1029/94JA01901.

Tuttle, S., B. Gustavsson, and B. Lanchester (2014), Temporal and spatial evolution of auroral electron energy spectra in a region surrounding the magnetic zenith, *J. Geophys. Res. Space Physics*, *119*, 2318–2327, doi:10.1002/2013JA019627.

Vasyliunas, V. M. (1968), A survey of low-energy electrons in the evening sector of the magnetosphere with OGO 1 and OGO 3, *J. Geophys. Res.*, *73*, 2839–2884, doi:10.1029/JA073i009p02839.

Vickrey, J. F., R. R. Vondrak, and S. J. Matthews (1981), The diurnal and latitudinal variation of auroral zone ionospheric conductivity, *J. Geophys. Res.*, *86*, 65–75, doi:10.1029/JA086iA01p00065.

Vickrey, J. F., R. R. Vondrak, and S. J. Matthews (1982), Energy deposition by precipitating particles and Joule dissipation in the auroral ionosphere, *J. Geophys. Res.*, *87*, 5184–5196, doi:10.1029/JA087iA07p05184.

Vondrak, R. R., and M. J. Baron (1977), A method of obtaining the energy distribution of auroral electrons from incoherent scatter radar measurements, in *Radar Probing of the Auroral Plasma*, edited by A. Brekke, pp. 315–330, Universitetsforlaget, Tromsøø-Oslo-Bergen, Tromsø, Norway.

Wallis, D. D., and E. E. Budzinski (1981), Empirical models of height integrated conductivities, *J. Geophys. Res.*, *86*, 125–137, doi:10.1029/JA086iA01p00125.

Watermann, J., O. de la Beaujardière, D. Lummerzheim, J. Woch, P. T. Newell, T. A. Potemra, F. J. Rich, and M. Shapshak (1994), The dynamic cusp at low altitudes: A case study utilizing viking, DMSP-F7, and sondrestrom incoherent scatter radar observations, *Ann. Geophys.*, *12*(12), 1144–1157, doi:10.1007/s00585-994-1144-7.

Zettergren, M., J. Semeter, P.-L. Blelly, and M. Diaz (2007), Optical estimation of auroral ion upflow: Theory, *J. Geophys. Res.*, *112*, A12310, doi:10.1029/2007JA012691.